Article

Multifunctional Dy$_2$NiMnO$_6$/Reduced Graphene Oxide Nanocomposites and Their Catalytic, Electromagnetic Shielding, and Electrochemical Properties

Bibhuti Bhusan Sahoo,[♦] Prasanta Kumar Sahoo,*,[♦] Vijayabhaskara Rao Bhaviripudi, Krushna Chandra Sahu, Abhishek Tripathi, Naresh Kumar Sahoo, Radhamanohar Aepuru, Vishwajit M. Gaikwad, Srikant Sahoo, Ashis Kumar Satpati, and Chuan-Pei Lee*

Read Online

ACCESS | Metrics & More | Article Recommendations

ABSTRACT: Multifunctional nanocomposites have shown great interest in clean energy systems and environmental applications in recent years. Herein, we first reported the synthesis of Dy$_2$NiMnO$_6$ (DNMO)/reduced graphene oxide (rGO) nanocomposites utilizing a hybrid approach involving sol−gel and solvothermal processes. Subsequently, we investigated these nanocomposites for their applications in catalysis, electromagnetic interference shielding, and supercapacitors. A morphological study suggests spherical-shaped DNMO nanoparticles of an average size of 382 nm that are uniformly distributed throughout the surface without any agglomeration. The as-prepared nanocomposites were used as catalysts to investigate the catalytic reduction of 4-nitrophenol in the presence of NaBH$_4$. DNMO/rGO nanocomposites demonstrate superior catalytic activity when compared with bare DNMO, with the rate of reduction being influenced by the composition of the DNMO/rGO nanocomposites. In addition, novel multifunctional DNMO/rGO was incorporated into polyvinylidene difluoride (PVDF) to develop a flexible nanocomposite for electromagnetic shielding applications and exhibited a shielding effectiveness of 6 dB with 75% attenuation at a frequency of 8.5 GHz compared to bare PVDF and PVDF-DNMO nanocomposite. Furthermore, the electrochemical performance of DNMO/rGO nanocomposites was investigated as an electrode material for supercapacitors, exhibiting the highest specific capacitance of 260 F/g at 1 A/g. These findings provide valuable insights into the design of DNMO/rGO nanocomposites with remarkable performance in sustainable energy and environmental applications.
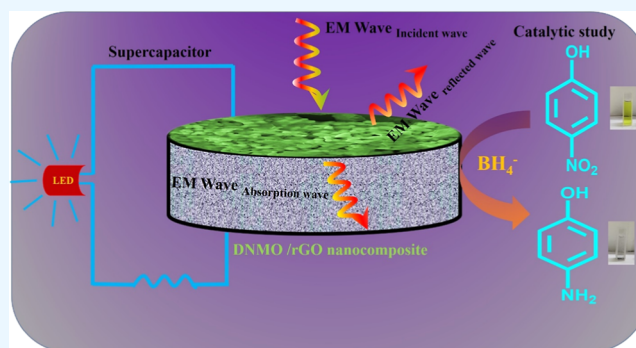
1. INTRODUCTION

The gradual increase of environmental issues and the increasing energy demand are contemporary challenges in our day-to-day lives, especially in the 21st century. The attention toward clean energy systems and environmental sustainability is gradually increasing to develop renewable energy sources, photocatalytic degradation, and efficient electromagnetic absorption systems.[1−3] Several technologies have been employed to build energy storage devices, such as batteries, supercapacitors, and water splitting, to meet energy demands. Recently, multifunctional hybrid nanostructures have emerged as a promising platform for energy and environmental applications due to their unique properties and potential for integration of multiple functionalities achieved by two or more components, such as metals,[4] semiconductors,[5] polymers,[6] and carbon-based materials,[7] which can be tailored to meet specific requirements. These multifunctional nanostructures have been used for a variety of applications, such as supercapacitors,[7]

electromagnetic shielding,[8] and catalytic reduction[9] to realize clean energy systems toward environment sustainability.

Common organic water pollutants such as dyes can easily pollute the environment and water bodies.[1] Several treatment methods are available for dye removals; moreover, adsorption is considered a promising treatment technique because of its excellent removal efficiency and low energy requirements. Recently, lanthanum cerate (La$_2$Ce$_2$O$_7$)-based perovskite has been synthesized for the degradation of food dye by studying the photocatalytic behavior by removing the carcinogenic and neurotoxic dye from the aqueous solution.[10] Likewise, a
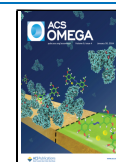
heterogeneous catalysis LaNiO$_{3-\delta}$ (LNO) perovskite oxides have been employed for the degradation of methyl orange (MO) azo dye with 94.3% efficiency at 5 ppm MO with 1.5 g/L LNO in aqueous solutions under dark ambient conditions.[11] Psathas et al. have adopted flame spray pyrolysis to prepare perovskite BiFeO$_3$-phase or mullite-type Bi$_2$Fe$_4$O$_9$-phase and used it for catalytic reduction of 4-nitrophenol (4-NP) to 4-aminophenol (4-AP) in the presence of NaBH$_4$.[12] The as-synthesized materials exhibit excellent catalytic activity toward 4-NP reduction that is comparable with best-performing noble-metal nanocatalysts. The nanocasting technique is used by Mhlwatika and Bingwa to synthesize ABO$_3$ perovskites (A = La or Sr, B = Co, Sn, Fe, or Al), and the as-prepared samples were used for the reduction of 4-nitrophenol (4-NP) by NaBH$_4$.[13] Among ABO$_3$ perovskites, SnAlO$_3$ showed a higher catalytic efficiency toward 4-NP.

Also, rare-earth-heavy and light perovskite oxide materials can be explored for a wide range of applications. For instance, the heavy rare earth elements, such as europium, gadolinium, terbium, dysprosium, and yttrium, can be realized as perovskite oxides. In our previous work, multiferroic flexible films of double perovskite Dy$_2$NiMnO$_6$ (DNMO) were prepared by incorporating DNMO particles in the polymeric matrix, which exhibited a large polarization and coercive field at room temperature with enhanced ferromagnetic nature and dielectric behavior with reduced dielectric loss.[14] On the other side, microwave absorbents were fabricated by oriented nickel (Ni) in the polyvinylidene fluoride (PVDF) with different Ni proportions and tested over a wide frequency range of 18−40 GHz and showed a shielding effectiveness of 20−35 dB due to the increase in the magnetic losses in the composites.[15] Combining the metal oxides with carbon-based and metal-dopant ingredients may improve the dielectric and magnetic losses due to the double attenuation mechanism for enhanced shielding performance.[2] Liu et al. adopted a hard template method using NaCl to synthesize a two-dimensional LaFeO$_3$/C composite. It has been noticed that A-site cation-deficient perovskites (La$_{0.62}$FeO$_3$/C) show excellent shielding performance of −26.6 dB at 9.8 GHz (X-band range) with a thickness of 2.94 mm among other samples because of induction of more dipoles polarization loss.[16] A 4-fold enhancement in EMI shielding of La$_{0.5}$Sr$_{0.5}$CoO$_{3-\delta}$ epoxy composite (4.7 dB at 10 GHz) was observed by Dijith et al. when it was screen printed with silver patterns on the top of the composite (22−31 dB at 8.2−18 GHz).[17] Sharma et al. fabricated N−La$_{0.85}$Sr$_{0.15}$CoO$_{3-\delta}$ (LSCO) nanoparticles incorporated carbon nanofiber-poly-dimethylsiloxane composite through a combination of electro-spinning and heat treatment processes. Twenty-five wt % CNFs incorporated LSCO exhibits maximum EMI shielding effectiveness of 45 dB at a thickness of 0.08 mm in a frequency range of 8.2−26.5 GHz due to the synergistic effect of both LSCO and CNFs, high interfacial polarization, and 3D electrically conductive network of LSCO and layer-by-layer and porous structure of CNFs.[18] Recently, carbon-based composite materials have been employed for microwave electromagnetic interference shielding (EMI) applications using 1D materials (CNTs, CNFs, etc.), 2D materials (rGO, MXenes, etc.), and 3D materials like carbon foam, graphene aerogels, etc. due to their exceptional flexible and conductive nature, excellent mechanical strength with impedance match-ing, and low densities.[19] Also, composite-based layered materials such as graphene, MXenes, and transition metal dichalcogenides were incorporated into the polymeric matrix

to improve the EMI shielding performance.[20] Especially, reduced graphene oxide (rGO) has been utilized due to its high surface area and high dielectric loss with a conducting nature for EM microwave applications. However, the low magnetic loss in the rGO limits the impedance match and results in a low EM shielding performance. Realizing the multifunctional nanostructures by heteroatom doping in graphene and also integrating the rGO with magnetic metal oxides could obtain excellent EM microwave absorption performance by overcoming the limitations of EMI shielding application.[21,22] For instance, 3D hierarchical faceted-iron oxide (f-Fe$_3$O$_4$) with carbon nanotubes (CNTs) on rGO hybrids has been reported by Kumar et al. for EMI shielding applications. The f-Fe$_3$O$_4$−CNT-rGO hybrid nanostructures has a synergetic effect of magnetic and dielectric losses to improve the EMI shielding performance to ∼25 dB at 1.0 mm thickness in a frequency region of 8.2−12.4 GHz.[22]

Furthermore, multifunctional nanostructures have been extensively used as electrode materials for supercapacitors as green energy storage devices due to their high specific power, long lifespan, quick charge−discharge rates, environmentally friendly, memory backup equipment, and low maintenance cost.[3,23−25] Moreover, it is essential to design electrode materials with a high active area, low carrier resistance, and consistent nanostructures for long cycles, which can be achieved by pseudocapacitive nanostructures, mainly metallic oxides and additional metal compounds like metal-sulfides and phosphides.[26,27] Kumar et al. synthesized 3D f-Fe$_3$O$_4$-rGO hybrid nanostructures and used them as electrode materials for supercapacitors. These carbon-based hybrid nanostructures displayed a slight initial drop of 8.6% (over 190 cycles) in the capacity and after that maintained good cyclic stability over 9500 cycles. The stable structure of the hybrid nanostructures, which provides easy pathways for electrolyte diffusion leads to long-term cyclic performance.[28]

In this context, perovskite oxides quickly gained attention due to their low cost, robust skeleton structure, high extraction density, inherent nature of the oxygen vacancies, and the ability to customize specific chemistry. In the past, perovskite oxides have been used as functional materials in energy-related applications especially supercapacitors because of their unique features such as electrochemical behavior with large diffusion rates and thermal stability.[29−32] Recently, Kumar et al.[31] reported double perovskite Ba$_2$FeCoO$_6$ as electrode material which evidenced a specific capacitance of approximately 820 F g^{-1} at a 3 A g^{-1}. Also, a multiferroic double perovskite Y$_2$NiMnO$_6$ (YNMO) has been reported by Alam et al.[33] which observed a capacitance value of 77.76 F g^{-1} at a 30 mA g^{-1}. In general, the rare-earth cations like La, Sm, and Dy at the R-site in the perovskite oxides normally do not contribute to the electronic structure but can impact the oxidation/valence states of Ni/Mn cations, the active area for electrochemical processes, porosity, and oxygen vacancies. The unusual charge storage capability has enabled the potential of perovskite oxides to improve the supercapacitor performance. Moreover, the poor conductivity and the unsatisfactory specific capacitance are serious drawbacks. The concept of hybrid perovskite oxides by integrating with carbon materials especially 2D graphene can enhance the mechanical, thermal, optical, and electrical properties due to the sp^2-hybridized carbon atoms. The higher electron mobility, excellent electrical conductivity, large surface area, intrinsic capacitance, and good stability of graphene can be successfully hybridized with
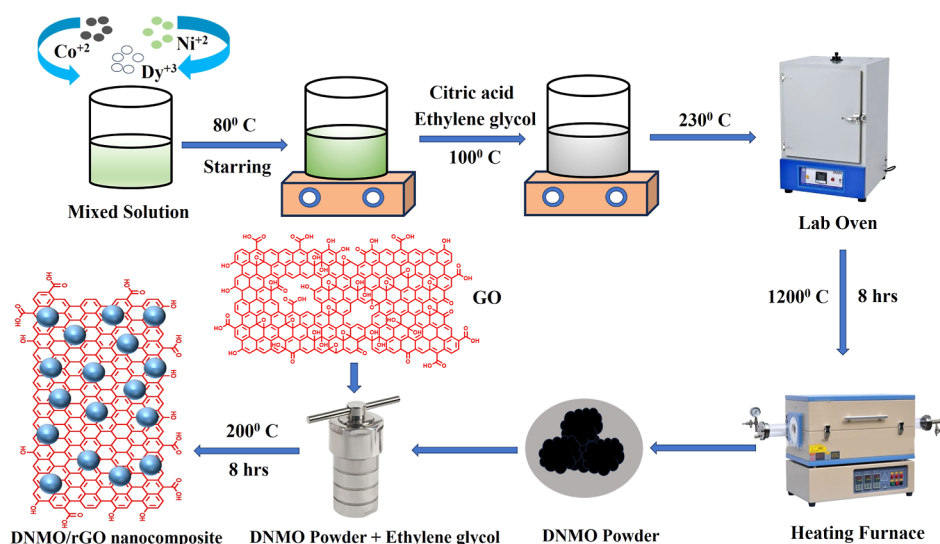
Figure 1. Schematic presentation of synthesis of the DNMO/rGO nanocomposite by a two-step solvothermal approach.

perovskite oxide and can be an excellent candidate with multifunctional properties for supercapacitor electrodes.[33,34] On the other hand, the multifunctional behavior in the hybrid perovskite oxides has been exploited for other applications as a radiation barrier in shielding electromagnetic waves; adaptive catalytic materials to degrade organic dyes via reduction reactions, allowing them to be exploited as adaptive catalytic materials. To date, the multifunctional behavior of Dy_2NiMnO_6 (DNMO)/rGO hybrid nanostructures for EMI, catalytic, and electrochemical behaviors has not been explored.

In this article, we report double perovskite Dy_2NiMnO_6 (DNMO) grown on graphene nanosheets (rGO) using a two-step approach to prepare multifunctional DNMO/rGO nanocomposites. The structure and morphology of the DNMO/rGO nanocomposites were systematically investigated by X-ray diffraction (XRD), Raman, FEG-scanning electron microscopy (SEM), energy-dispersive X-ray spectroscopy (EDS), and X-ray photoelectron spectroscopy (XPS). The catalytic activity of as-synthesized DNMO/rGO nanocomposites and bare DNMO were investigated toward 4-NP reduction as a model reaction in the presence of $NaBH_4$. Thereafter, the DNMO/rGO nanocomposites were incorporated into a polymeric matrix to study the shielding effectiveness for EMI shielding application. The electrochemical performance of DNMO/rGO nanocomposites was examined as electrode materials for supercapacitor applications by cyclic voltammetry (CV) in 5 M KOH as an electrolyte. The as-prepared DNMO/rGO nanocomposite showed the highest specific capacitance of 260 F/g at a current density of 1 A/g.

2. EXPERIMENTATION SECTION

2.1. Materials. Dysprosium oxide (99.9% purity), nickel acetate (98% purity), manganese acetate (98% purity), and natural flake graphite (particle size 45 mm) were purchased from Sigma-Aldrich. All other chemicals were purchased from Merck Specialties Private Limited, India. Double distilled water (DDI) was utilized for the preparation of aqueous solutions.

2.2. Synthesis of DNMO. DNMO was synthesized by the sol−gel method using dysprosium oxide, nickel acetate, and manganese acetate in a stoichiometric ratio. To prepare solution 1, dysprosium oxide (2.151 g) was dissolved in DDW

containing nitric acid under constant stirring. To prepare solution 2, nickel acetate (1.435 g) was dissolved in DDW with constant stirring. To prepare solution 3, manganese acetate (1.413 g) was dissolved in DDW with constant stirring. Then, the precursor solutions 1, 2, and 3 were mixed and stirred for 2 h and maintained temp 80 °C. Thereafter, 5 g of citric acid was added into it to form a metal-citrate complex. Afterward, 5 mL of ethylene glycol was added to it. During this whole process, the mixed solution maintained clear and constant stirring, and then, the resultant solution was heated at 100 °C to form a viscous gel. A few minutes later, the solution turned rapidly into a gel. The resultant gel was further heated at 230 °C until the formation of fine powder. After that, the powder was ground and annealed at 1200 °C for 8 h to obtain the final product.

2.3. Synthesis of DNMO/rGO Nanocomposite. Graphene oxide (GO) was prepared from the natural flake graphite (particle size 45 mm) GO was prepared by Modified Hummers' method.[35] Different amounts of DNMO and GO were added into a solution of ethylene glycol (EG), followed by sonication for 30 min, and stirred for 1 h to form a clear solution. Then, the as-prepared solution was transferred into a 100 mL Teflon-lined SS autoclave and kept at 200 °C for 12 h. After the autoclave was cooled to room temperature, the as-prepared sample was washed with deionized water and ethanol several times and dried at 65 °C, yielding the DNMO/rGO nanocomposite. The DNMO/rGO nanocomposites with different weight ratios of 50:100 and 100:50 were prepared by the same hydrothermal methods, and the as-prepared samples are named DNMO/rGO (50:100) and DNMO/rGO (50:100) nanocomposites, respectively. Figure 1 shows the detailed schematic presentation of the synthesis of DNMO/rGO nanocomposite.

2.4. Instrumentation and Measurements. Phase purity and crystal structure of the as-prepared samples were determined by using a Philips powder diffractometer (PW 3040/60) with Cu Kα radiation (λ = 0.15406 nm). Lab RAM HR 800 Micro laser Raman system with an Ar⁺ laser of wavelength 519 nm is used to record Raman spectra of the as-prepared samples. MULTILAB from Thermo VG Scientific with Al Kα radiation as a monochromator is performed to analyze the XPS spectrum, and the peaks are deconvoluted and
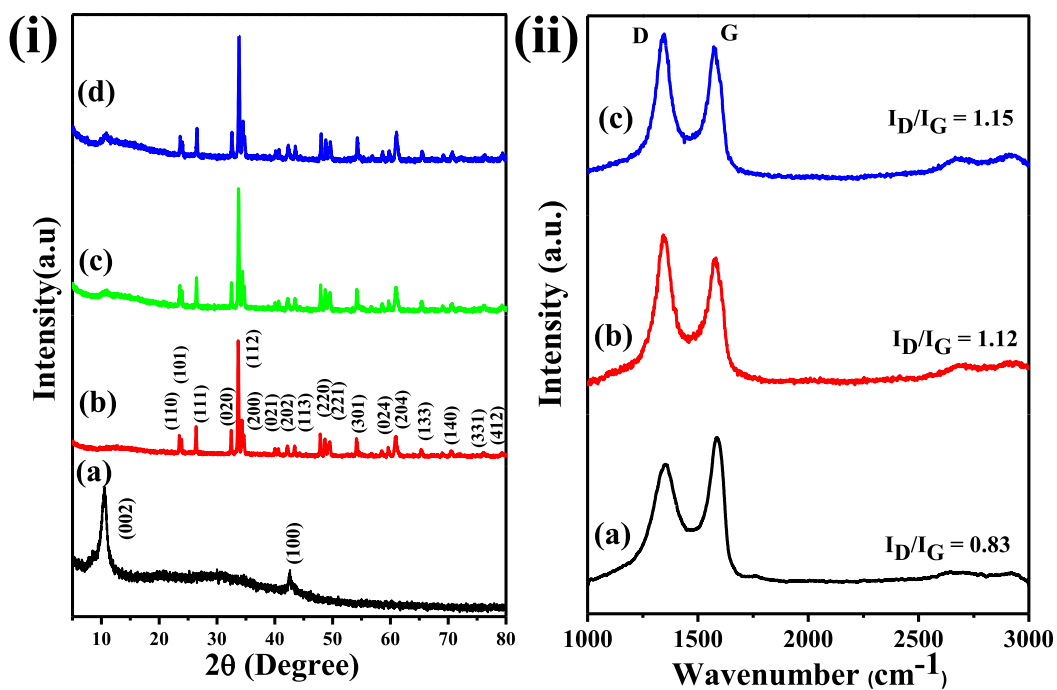
Figure 2. (i) XRD patterns of (a) GO, (b) bare DNMO, (c) DNMO/rGO (100:50), and (d) DNMO/rGO (50:100) nanocomposites and (ii) Raman spectra of (a) GO, (b) DNMO/rGO (100:50), and (c) DNMO/rGO (50:100) nanocomposites.
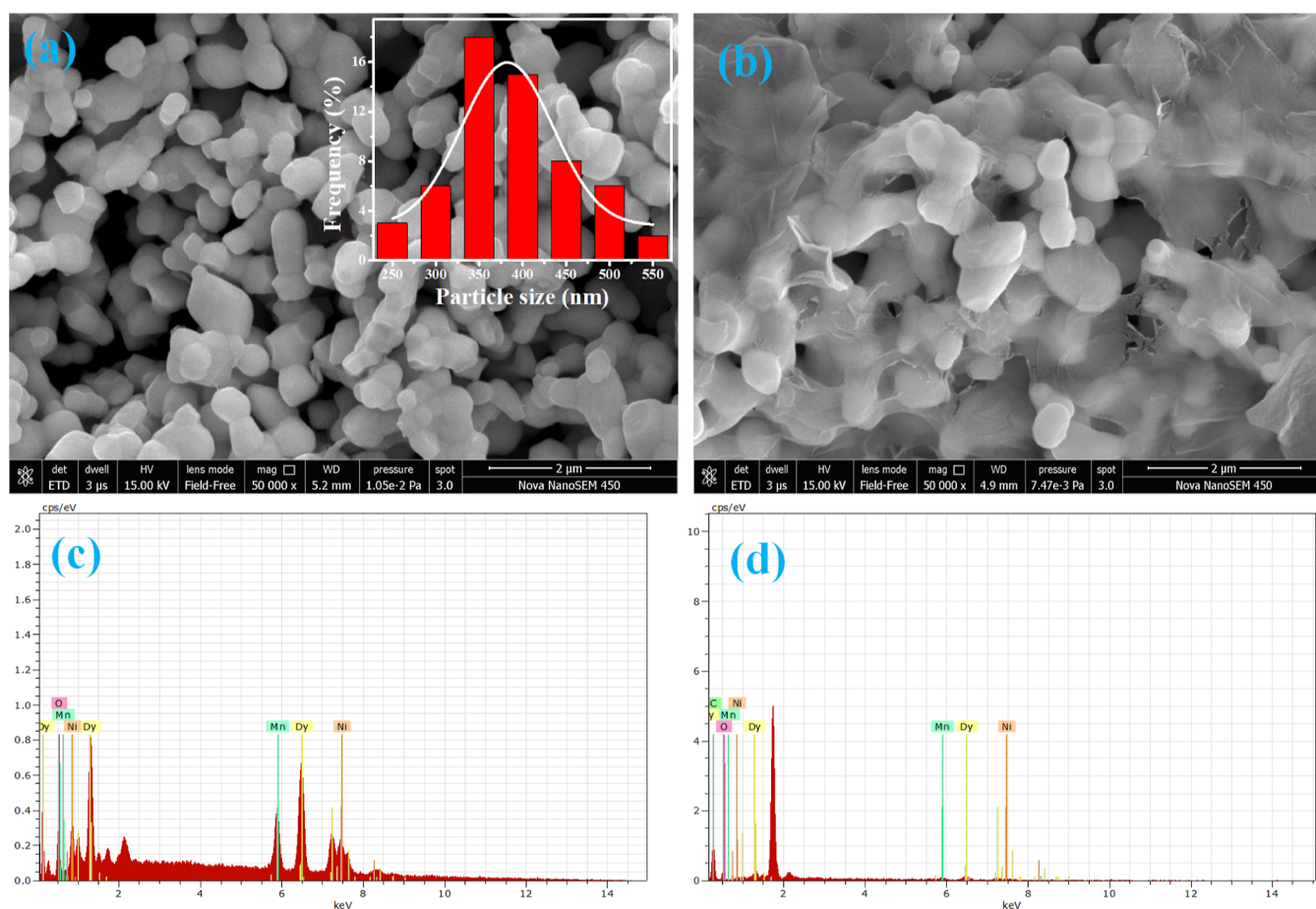

Figure 3. FEG-SEM images of (a) bare DNMO (inset: particle size distribution histogram of DNMO), (b) DNMO/rGO (50:100) nanocomposite, EDS spectrum of (c) bare DNMO, and (d) DNMO/rGO (50:100) nanocomposite.
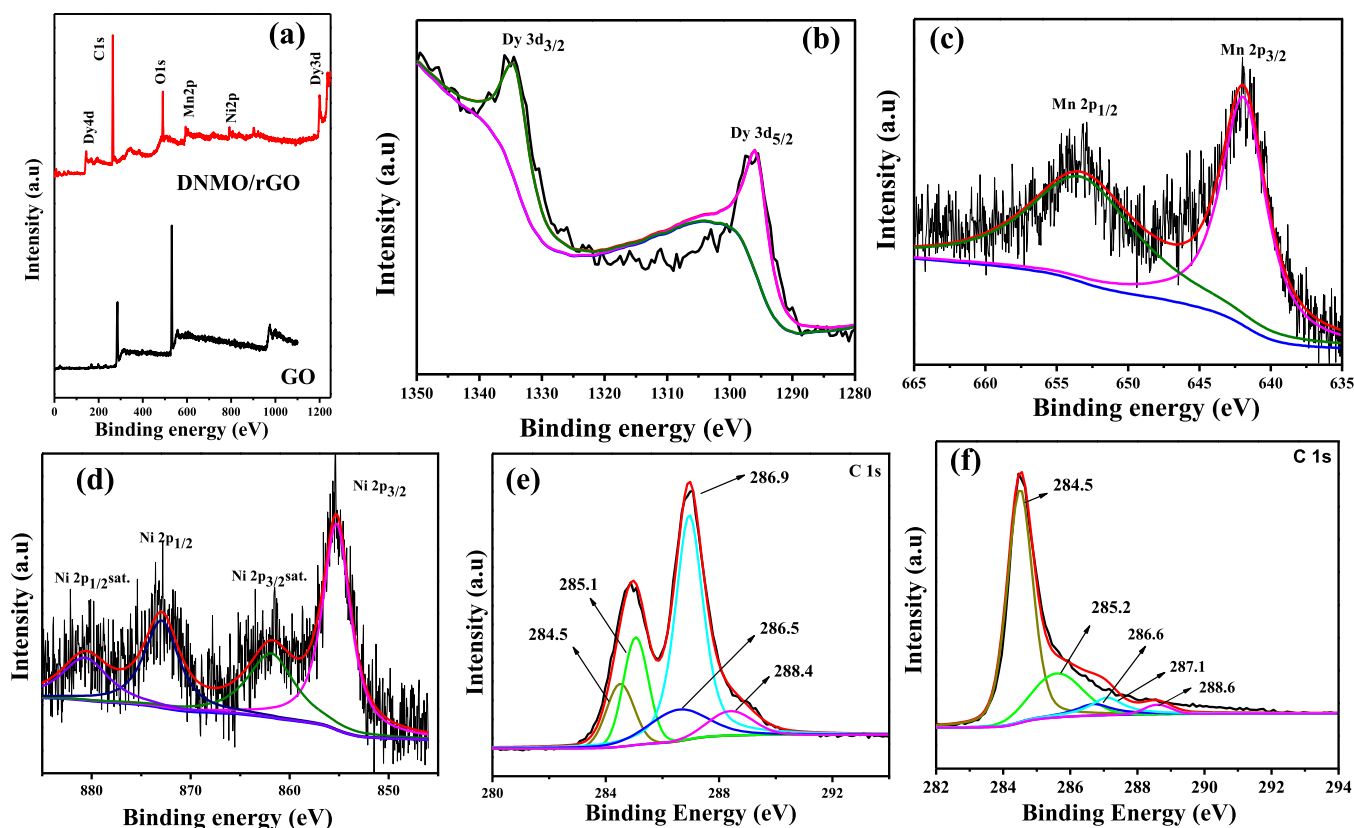
Figure 4. (a) XPS survey spectrum of GO and DNMO/rGO (50:100) nanocomposite, high-resolution (b) Dy 3d, (c) Mn 2p, (d) Ni 2p, and C 1s XPS spectra of (e) GO and (f) DNMO/rGO (50:100) nanocomposite.

fitted by using XPSPeak41 software and Lorentzian−Gaussian functions, respectively. The morphology and elemental compositions of the as-prepared samples were examined by using field emission SEM (FE-SEM, JEOL, model JSM-7600F) and energy-dispersive X-ray spectroscopy (EDX), respectively.

3. RESULTS AND DISCUSSION

XRD patterns of GO, bare DNMO, and the DNMO/rGO nanocomposite are displayed in Figure 2. As shown in Figure 2(i)a, the diffraction peaks at $2\theta°$ values 10.4 and 43.5 correspond to the (002) plane of short-range ordered stacked graphene sheets of GO and hcp structure of carbon.[35] The diffraction peaks at $2\theta°$ values of nearly 23.6, 23.9, 26.5, 32.6, 33.7, 34.5, 40.2, 42.3, 43.5, 48.1, 44.5, 54.2, 59.7, 61.1, 65.5, 70.7, 76.4, and 78.8° in Figure 2(i)b−d are ascribed to the (110), (101), (111), (020), (112), (200), (021), (202), (113), (220), (221), (302), (024), (204), (133), (140), (331), and (412) diffraction planes of monoclinic structure of DNMO with $P2_1/n$ space group.[36] However, no apparent characteristic peaks of rGO in the DNMO/rGO nanocomposites are observed in Figure 2(i)c,d, which may be because of suppresses of (002) diffraction peak due to high-intensity peaks of DNMO or restacking of graphene sheets prevented due to incorporation of DNMO into rGO sheets.[35]

Raman spectroscopy is mainly used to determine the electronic and structural properties of carbonaceous materials and defects in sp² carbon materials. Raman spectra for bare GO and DNMO/rGO (100:50) and DNMO/rGO (50:100) nanocomposites were recorded at room temperature in the range 1000−3000 cm⁻¹. As shown in Figure 2(ii)a−c, All the samples show characteristic D peaks, and the G peaks nearly at

1343 and 1582 cm⁻¹, respectively. The D peak is linked to defects and atomic disorder, while the G peak's intensity is linked to carbon's sp² vibration.[37] The average size of the sp² domains is evaluated from the D to G band intensity ratio (I_D/I_G). The I_D/I_G intensity ratios of GO, DNMO/rGO (100:50), and DNMO/rGO (50:100) nanocomposites are 0.83, 1.12, and 1.14, respectively. The higher I_D/I_G intensity ratio in DNMO/rGO (100:50) and DNMO/rGO (50:100) nanocomposites suggested a possible removal of most of the oxygenic functional groups during the reduction process and successful conversion of GO to rGO during the hydrothermal treatment.[38]

Morphology and elemental composition of bare DNMO and DNMO/rGO (50:100) nanocomposite were investigated through field emission SEM (FEG-SEM) and EDS. As shown in Figure 3a, DNMO exhibits spherical-shaped particles with an average size of 382 nm in a well-connected manner (inset). In the case of the DNMO/rGO (50:100) nanocomposite in Figure 3b, spherical-shaped DNMO nanoparticles of average sizes of 382 nm are uniformly distributed throughout the surface without any agglomeration. Figure 3c,d, shows the EDS spectrum of bare DNMO and DNMO/rGO (50:100) nanocomposite. The EDS spectrum of bare DNMO confirms the existence of elementals Dy, O, Mn, and Ni, indicating successful synthesis of DNMO. In addition to Dy, O, Mn, and Ni, C is present in the DNMO/rGO (50:100) nanocomposite, confirming the presence of rGO.

Details of the surface electronic state of the elements present in the GO and DNMO/rGO (50:100) nanocomposite were investigated by XPS analysis. Figure 4a shows the survey spectrum of GO and the DNMO/rGO (50:100) nano-
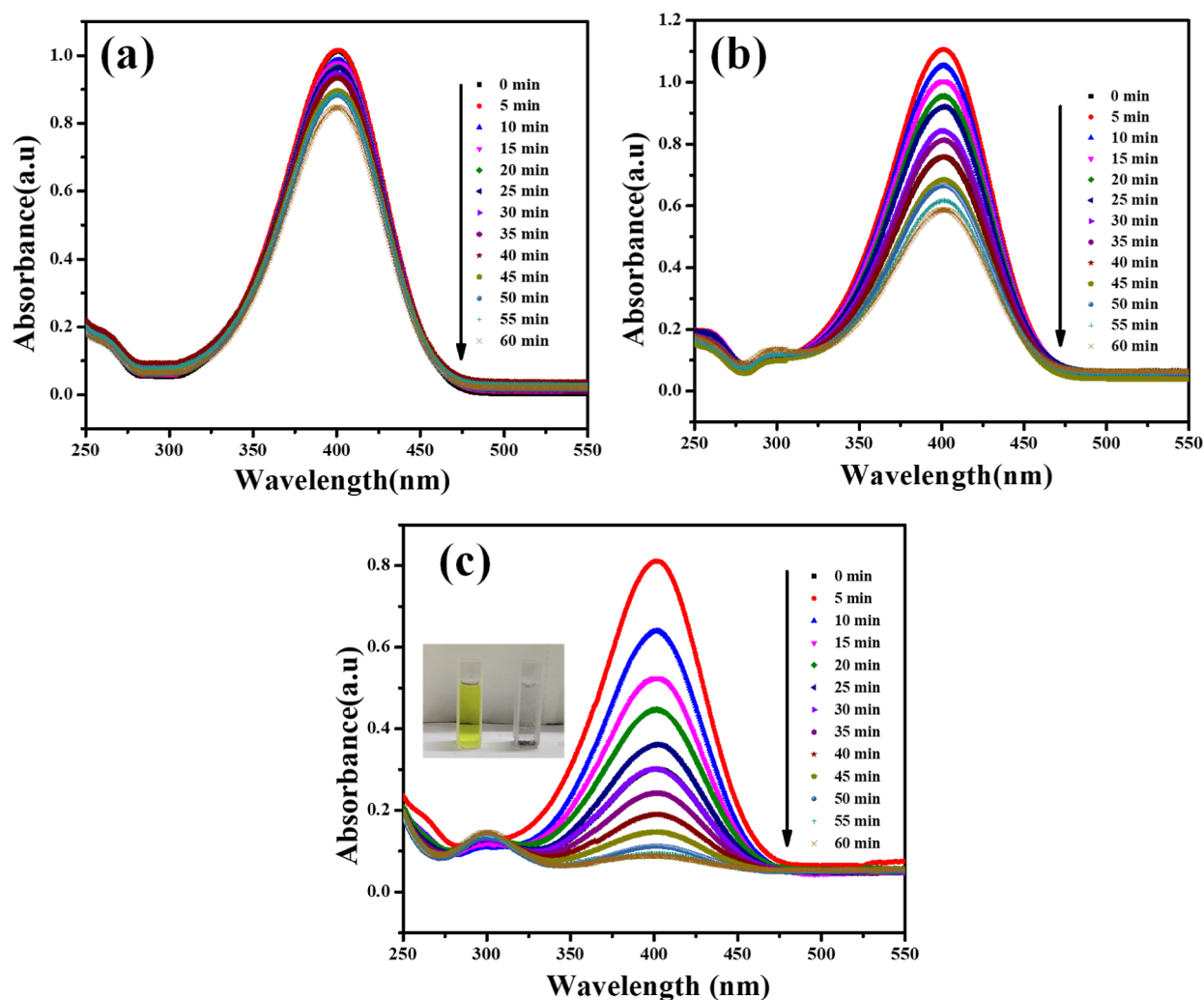
Figure 5. UV−vis absorption spectra of 4-NP reduction by NaBH$_4$ in the presence of (a) DNMO, (b) DNMO/rGO (100:50), and (c) DNMO/rGO (50:100) catalysts (inset: discoloration of 4-NP).

composite. As shown in Figure 4a, survey spectra of GO contain C1 s and O1 s peaks, whereas Dy 3d, Ni 2p, and Mn 2p peaks are observed along with C1 s and O 1s speak in the survey spectrum of DNMO/rGO (50:100) nanocomposite, indicating the successful formation of DMNO in the DNMO/rGO (50:100) nanocomposite. In addition, the intensity of the C 1s peak versus the O 1s peak of DNMO/rGO (50:100) nanocomposite is higher than that of GO, indicating reduction of GO to rGO. The two distinct peaks at 1296.1 and 1334.6 eV in the Dy 3d spectrum in Figure 4b correspond to the binding energies of Dy 3d$_{5/2}$ and Dy 3d$_{3/2,}$ attributed to the presence of Dy^{3+} ions.[39] In the case of Mn 2p high-resolution XPS spectrum in Figure 4c, the deconvoluted peaks at binding energy 642.1 and 653.4 eV correspond to spin−orbit splitting binding energy of 2p$_{3/2}$ and 2p$_{1/2}$ levels, ascribing to the coexistence of Mn^{3+} and Mn^{4+} ions in the DNMO/rGO (50:100) nanocomposite.[40] Figure 4d shows the high-resolution XPS spectrum of Ni 2p level exhibiting binding energy of 855.3 and 872.9 eV corresponding to 2p$_{3/2}$ and 2p$_{1/2}$ signals of Ni^{2+}.[33] The deconvoluted C 1s peak of GO and DNMO/rGO (50:100) nanocomposite is shown in Figure 4e,f, respectively. Four peaks of C═C, C═O, C═O, and C═O−C═O can be observed at binding energies of 284.5, 285.5, 286.8, and 288.4 eV in Figure 4e, indicating the successful

oxidation of graphite in the oxidation process. An abundance in oxygen-containing functional groups on GO. However, the removal of oxygenic functional groups and reduction of GO to rGO in the DNMO/rGO (50:100) nanocomposite is confirmed by the decrease in peak intensities of the oxygenic functional groups in the C 1s spectrum of the DNMO/rGO (50:100) nanocomposite.[38]

3.1. Catalytic Study. A crucial organic process for the production of numerous industrial goods is that in the presence of NaBH$_4$, nitroaromatic compounds are reduced to the corresponding amine molecules. It is a crucial step in the manufacturing of several crucial industrial products, including corrosion inhibitors, photographic developers, and analgesic and antipyretic medications.[9,41] It is crucial for industry and the environment that this catalytic reduction reaction occurs. Additionally, it serves as a reaction in assessing the catalytic effectiveness of different catalysts. It is well-known that NaBH$_4$ may catalytically reduce 4-NP to 4-amino phenol (4-AP) in the presence of various nanoparticles serving as catalysts. It is generally known that in a basic media, 4-NP absorbs at 400 nm. As the reduction reaction progresses, it has been observed that the strength of 4-NP's absorption at 400 nm diminishes progressively, accompanied by the emergence of a new peak at 300 nm. This suggests the formation of 4-AP during the
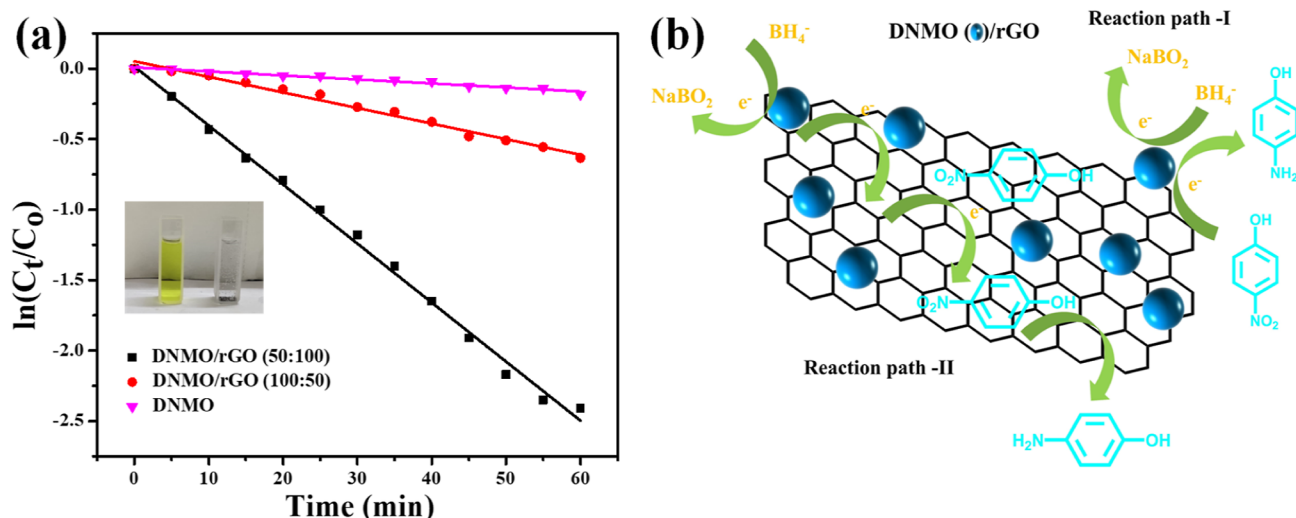
Figure 6. (a) Plot of ln C_t/C_0 vs time for the catalytic reduction of 4-NP in the presence of DNMO, DNMO/rGO (100:50), and DNMO/rGO (50:100) catalysts (inset: discoloration of 4-NP). (b) Possible 4-NP reduction mechanism by the DNMO/rGO nanocomposite in the presence of NaBH$_4$.

reduction process. During the reduction process, the rate of electron transfer is influenced by the reactant's (4-NP) adsorption on the catalyst surface, interfacial electron transfer, and product desorption from the surface of the catalyst.[4,42] The reduction process can be observed, where the color of the solution during reaction progressively fades over a period of time, and it is used as a model reaction to evaluate the catalytic efficiency of different catalysts.

The catalytic activity of as-synthesized DNMO, DNMO/rGO (100:50), and DNMO/rGO (50:100) were investigated using NaBH$_4$ as a reducing agent, allowing them to be exploited as adaptive catalytic materials. For the reduction procedure, a new aqueous solution of NaBH$_4$ of 1.5 M and 4-nitrophenol of 5 mM was typically prepared separately using Milli-Q water. After 3 mL of freshly generated 1.5 M NaBH$_4$ solution was combined with 100 mL of Milli-Q water, 20 mg of each catalyst was added to various reaction solutions. Then, 2 mL of freshly produced 4-NP were mixed individually with the above-mentioned combination solution. 1 mL of the reaction solution was withdrawn every 5 min and mixed with 1 mL of Milli-Q water. Through examination of the UV−vis spectra of the corresponding reaction solutions, the reduction of 4-NP was observed. The entire catalytic process was performed at room temperature. By conducting trials under the same settings but stopping them at certain points, it was possible to predict how 4-NP would degrade over time. Measurements were carried out at room temperature, typically for 0 to 60 min, and with DNMO, DNMO/rGO (100:50), and DNMO/rGO (50:100) catalysts. Through the use of UV spectrophotometry, the degradation of 4-NP in the presence of catalysts was also examined. In some instances, the rate of 4-NP degradation over time was calculated to highlight the significance of several factors. Figure 5 shows the time-dependent absorption spectra of the 4-NP reduction in the presence of DNMO, DNMO/rGO (100:50), and DNMO/rGO (50:100) catalysts at room temperature at a regular interval of 5 min for 60 min. As shown in Figure 5, the maximum absorbance was observed at 400 nm during 4-NP reduction by NaBH$_4$ in the presence of DNMO, DNMO/rGO (100:50), and DNMO/rGO (50:100) catalysts. In all four cases, as the reduction reaction proceeds with time,

the absorption intensity of the 4-NPs at 400 nm gradually decreases, while a new peak is produced at 300 nm. This shows that NABH$_4$ reduces 4-NP to form colorless (inset: Figure 5c) in the presence of the DNMO, DNMO/rGO (100:50), and DNMO/rGO (50:100) catalysts. It is noticed that DNMO/rGO (50:100) catalysts show the highest degradation rate of 4-NP as compared to the DNMO and DNMO/rGO (100:50), and the order of reduction rate is DNMO/rGO (50:100) > DNMO/rGO (100:50) > DNMO.

The kinetics for 4-NP reduction appeared to follow the pseudo-first-order with excess use of NaBH$_4$.[43,44] As a result, the kinetics for this reduction process is as follows

$$kt = \ln C_0 - \ln C = \ln A_0 - \ln A \qquad (1)$$

where k denotes the rate constant, C_0 and C are the 4-NP concentrations at $t = 0$ and $t = t$, respectively. At periods $t = 0$ and $t = t$, A_0 and A are the absorbances of 4-NP ($\lambda_{max} = 400$ nm).[37] The absorbance ratio (A_t/A_0) is used to calculate the ratio of C_t to C_0 (C_t/C_0) at 400 nm. As shown in Figure 6a, the ln(C_t/C_0) versus time (t) plots for all catalysts are linearly correlated, which is evidence for the pseudo-first-order reaction. Pseudo-first-order rate constant (k) was investigated based on the slope of the linear plot for 4-NP reduction in the presence of four distinct catalysts and are given in Table 1. A shown in Figure 6a, the rate of catalytic reduction in the order DNMO/rGO (50:100) > DNMO/rGO (100:50) > DNMO.

We suggest a tenable mechanism for the reduction of 4-NP in the presence of DNMO/rGO nanocomposites as catalysts based on the aforementioned experimental observation, and Figure 6b illustrates this. In our work, the reduction of 4-NP in the presence of NaBH$_4$ and DNMO/rGO nanocomposites can be attributed to two probable reaction pathways. In reaction

Table 1. Rate Constants and the Correlation Coefficients for the Reduction of 4-NPs in the Presence of Various Catalysts

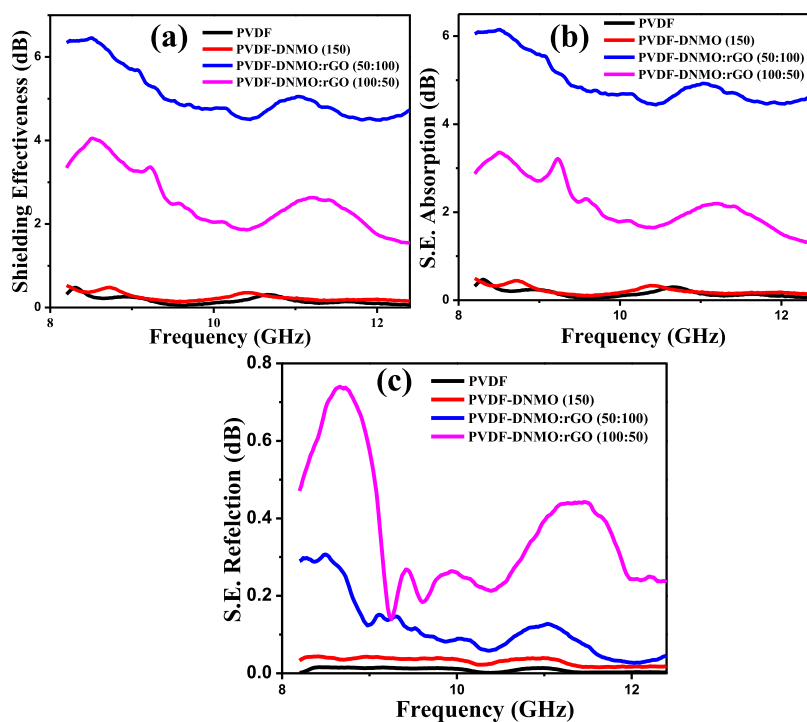|	DNMO	DNMO/rGO (100:50)	DNMO/rGO (50:100)
k (10^{-3}) min^{-1}	2.85	11.06	41.88
R^2	0.96993	0.9839	0.99573

Figure 7. EMI shielding (a) effectiveness, (b) absorption, and (c) reflection of PVDF, PVDF-DMO, PVDF-DNMO/rGO (50:100), and PVDF-DNMO/rGO (100:50) nanocomposites.

path-1, (a) NaBH$_4$ is oxidized to BO$_2^-$, which is initiated by the transfer of electrons from BH$_4^-$ ions to the DNMO nanoparticle. (b) The general reaction pathway produces 4-AP after the electrons are transferred to 4-NP through direct interaction with DNMO nanoparticles.[9,37] Reaction path-II, (a) begins with the oxidation of NaBH$_4$ to BO$_2^-$ and the transfer of electrons from BH$_4^-$ ions to DNMO nanoparticles. (b) Due to π–π stacking interactions, graphene sheets with a large specific surface area significantly increase the likelihood of π-rich 4-NP molecules adhering. By raising the local concentration of 4-NP, this adsorption aids in the electron capture process of DNMO nanoparticles. DNMO nanoparticles receive a large injection of electrons from the donor BH$_4^-$, which is subsequently transferred to graphene sheets. (c) These electrons are swiftly transported to acceptor 4-NP by the conductive graphene surface next to DNMO nanoparticles through an extended π-conjugation structure, resulting in the formation of 4-AP. (d) Lastly, 4-AP, which is created during the reduction process, is desorbed from the graphene sheets.[9,37] Therefore, the higher catalytic reduction of DNMO/rGO nanocomposites as compared to bare DNMO is because of synergistic effects of rGO and DNMO such as (i) the π–π stacking interaction between 4-NPs and rGO invites more number of 4-NPs molecules on the surface of the catalysts leads to higher adsorption, (ii) the conductive rGO surface adjacent to DNMO enhances the electron density in the vicinity of DNMO, leads to increase in electron-uptake by 4-NPs, and (iii) improvement of catalytic activity of DNMO due to prevention of agglomeration of DNMO by RGO sheets and increase in chemical stability of DNMO.[37] The highest catalytic activity of the DNMO/rGO (50:100) as compared to DNMO/rGO (100:50) is due to the higher content of rGO in the DNMO/rGO (100:50) composite.

3.2. Electromagnetic Interference Shielding Property.
The shielding properties by electromagnetic interference of the

samples of thickness approximately 0.3 mm in X band (8.2–12.4 GHz) of dimensions 2.1 × 1.01 cm^2 were analyzed by quantifying the S parameters (S_{11}, S_{12}, S_{21}, and S_{22}) through the vector network analyzer, which are used in measuring shielding effectiveness (SE).[6]

$$SE(dB) = -10 \log\left[\frac{P_I}{P_T}\right] \tag{2}$$

where the incident power and transmitting powers are expressed as P_I and P_T, respectively.

$$SE(dB) = SE_R + SE_A \tag{3}$$

where SE_R and SE_A are the shielding effectiveness by reflection and shielding effectiveness by absorption, respectively, which are given by

$$SE_R = -10 \log(1 - R), \quad SE_A = -10 \log\left[\frac{T}{(1-R)}\right]$$

in which $R = |S_{11}|^2$ and $T = |S_{21}|^2$. Here S_{11} represents the power received at antenna 1 in relation to the incident power to antenna 1, while S_{21} represents the power received at antenna 2 relative to the incident power to antenna 1.

The shielding effectiveness by reflection and absorption can be expressed in terms of dielectric constant (ε), conductivity (σ'), and permeability (μ') as

$$SE_R = -10 \log\left[\frac{\sigma'}{16\omega\mu'\varepsilon_0}\right], \quad SE_A = -10 \log\left[\frac{\sigma'\omega\mu'}{2}\right]^{1/2} \tag{4}$$

where $\sigma' = \varepsilon_0\omega\varepsilon''$, in which ω is the frequency, ε_0 is the vacuum permittivity = 8.854 × 10^{-12} F/m, and ε'' is the imaginary part of complex permittivity.

Figure 7a shows shielding effectiveness of PVDF, PVDF-DMO, and PVDF-DNMO/rGO nanocomposites. Among all, PVDF-DNMO/rGO (50:100) nanocomposite shows better performance than others by showing shielding effectiveness of approximately SE 6 dB suggests 75% of input EM wave getting attenuated whereas only PVDF and DNMO showed almost 0 dB means no shielding at all. The increment in percentage of rGO from 0 to 100 weight in DNMO by keeping the overall weight percentage of filler DNMO-rGO same in PVDF leads to an increment in shielding effectiveness from 0 to 6 dB, which means 75% of input electromagnetic wave attenuation. Shielding is mainly contributed from absorption and reflection and internal multiple reflections (Figure 7b,c). For the sample of PVDF-DNMO/rGO (50:100) SE is very high due to absorption by graphitic structure and interconnected networks of rGO and DNMO, leading to increasing conductivity and loss by high internal multiple reflections and finally results in the high shielding effectiveness. SE value for other samples is less due to dissipation of energy and nonuniformity and anomalous behavior of the filler in the polymer matrix causes a reduction in SE.[45,46]

Moreover, the shielding by reflection (Figure 7c) is due to the interaction of mobile carriers (free electrons) of rGO with electromagnetic fields in the radiation. On the other hand, the multiple reflections are caused at various interfaces and surfaces due to the presence of rGO in the PVDF-DNMO/rGO composites having a large surface or interface area. Similar observations were reported in our previous work and also in the work by Kumar et al. where the presence of rGO show multiple peaks in the frequency range.[22,47] The 2D layered structure of rGO improves multiple reflections and scattering of electromagnetic waves among their nanosheets. Also, DNMO which is a rare-earth-metal oxide double perovskite, has ferromagnetic and dielectric properties. Combining these oxides with rGO may improve the dielectric and magnetic losses due to the double attenuation mechanism due to the conductivity and dielectric and magnetic losses in the composites enhanced shielding performance. Therefore, the use of rGO−Dy$_2$NiMnO$_6$ in conjunction with polymers helps to tune the EMI field absorption and improves the mechanical flexibility. The electrical conductivity contributes in both the reflection and absorption parts and is correlated with skin depth δ at which the strength of the EM wave is diminished to 1/e times the original value. The skin depth is expressed as in terms of conductivity and SE$_A$.[22,48]

$$\delta = 8.68 \frac{t}{SE_A} \quad (5)$$

$$\delta = \frac{1}{\sqrt{\pi f \mu \sigma}} \quad (6)$$

where f is the frequency of applied waves, μ is the permeability of material, and σ is the conductivity of material.

Table 2 shows the SE at a frequency of 8.5 GHz. The high shielding effectiveness for sample PVDF-DNMO/rGO (50:100) was majorly influenced by phenomenon of absorption and interior multiple reflections in the composite films. This could be due to the absorption of EM waves by 2D graphitic layered structure by rGO and interconnected networks between DNMO and rGO. Whereas other concentrations of DNMO/rGO samples, show less EMI shielding because of low rGO concentration and availability of a smaller number of dielectric and magnetic dipoles, which

Table 2. Comparative Shielding Performance of the As-Prepared Samples

name of sample	SE at frequency of 8.5 GHz (dB)
PVDF	0.2
PVDF-DNMO	0.5
PVDF-DNMO/rGO (50:100)	6
PVDF-DNMO/rGO (100:50)	4

decreased the shielding value. Another possible explanation might be due to the aggregation of DNMO/rGO fillers within the PVDF, inducing a tunneling effect that results in an impedance mismatch between the fillers and the PVDF matrix. Thus, it stands as one of the prior studies that successfully attained high shielding performance by optimizing the filler loading in the composites. Thus, PVDF-DNMO/rGO composites evaluated for EMI shielding and sample of PVDF-DNMO/rGO (50:100) showed a better performance by showing SE of 6 dB loss means 75% of input EM wave gets attenuated.

3.3. Electrochemical Studies. Furthermore, the electrochemical properties of the DNMO/rGO (50:100) and DNMO/rGO (100:50) nanocomposites have been investigated by CV. A Biologic instrument (VSP-200) with a three-electrode setup was used to investigate the CV of the as-prepared samples. Glassy carbon with a 3 mm diameter was used as the working electrode, whereas platinum wire and an aqueous alkaline Hg/HgO electrode were used as the auxiliary and reference electrodes. An ink was prepared by mixing an optimized amount of electrode material and Nafion in an ethanol solution. Then, an optimized amount of ink was drop-cast on the mirror-polished glassy carbon before measurement. CV measurements were carried out in 5 M KOH as the electrolyte at scan rates of 1,2, 5, 10, 25, 50, 80, and 100 mV/s with a potential window from 0.1 to 0.5 V. The comparison of different CV curves of DNMO/rGO (50:100) and DNMO/rGO (100:50) in 5 M KOH electrolyte at a scan rate of 100 mV/s with a potential range of 0.1−0.5 V in Figure 8a. The enclosed area of the CV curve of the DNMO/rGO (50:100) electrode is greater than that of the DNMO/rGO (100:50) electrode, showing higher performance. Figure 8b,c show the CV curves of DNMO/rGO (100:50) and DNMO/rGO (50:100) nanocomposites in 5 M KOH electrolyte at a scan rate of 1,2, 5, 10, 25, 50, 80, and 100 mV s^{-1} with a potential range of 0.1−0.5 V. The oxidation peak and corresponding reduction peaks appeared in both the CV curves and current increases with scan rates, signifying pseudocapacitive nature and significant electrochemical reversible behavior with desirable capacitance.[49]

The specific capacitance of DNMO/rGO (50:100) and DNMO/rGO (100:50) nanocomposite electrodes can be investigated from the CV curves as expressed by the relation[38]

$$C_s = \frac{Q}{m\nu(V_c - V_a)} = \frac{1}{m\nu(V_c - V_a)} \int_{V_a}^{V_c} I(V)dV \quad (7)$$

where C_s is the specific capacitance of the deposited electroactive material, ($F\ g^{-1}$), "m" is the mass load of the electroactive materials, "ν" is the scan rate, $V_c - V_a$ is the potential window, and $I(V)$ is the response current. The average charge (Q) during the forward/backward potential scan is obtained from the integration of the response current during the charge or discharge of the CV curve.
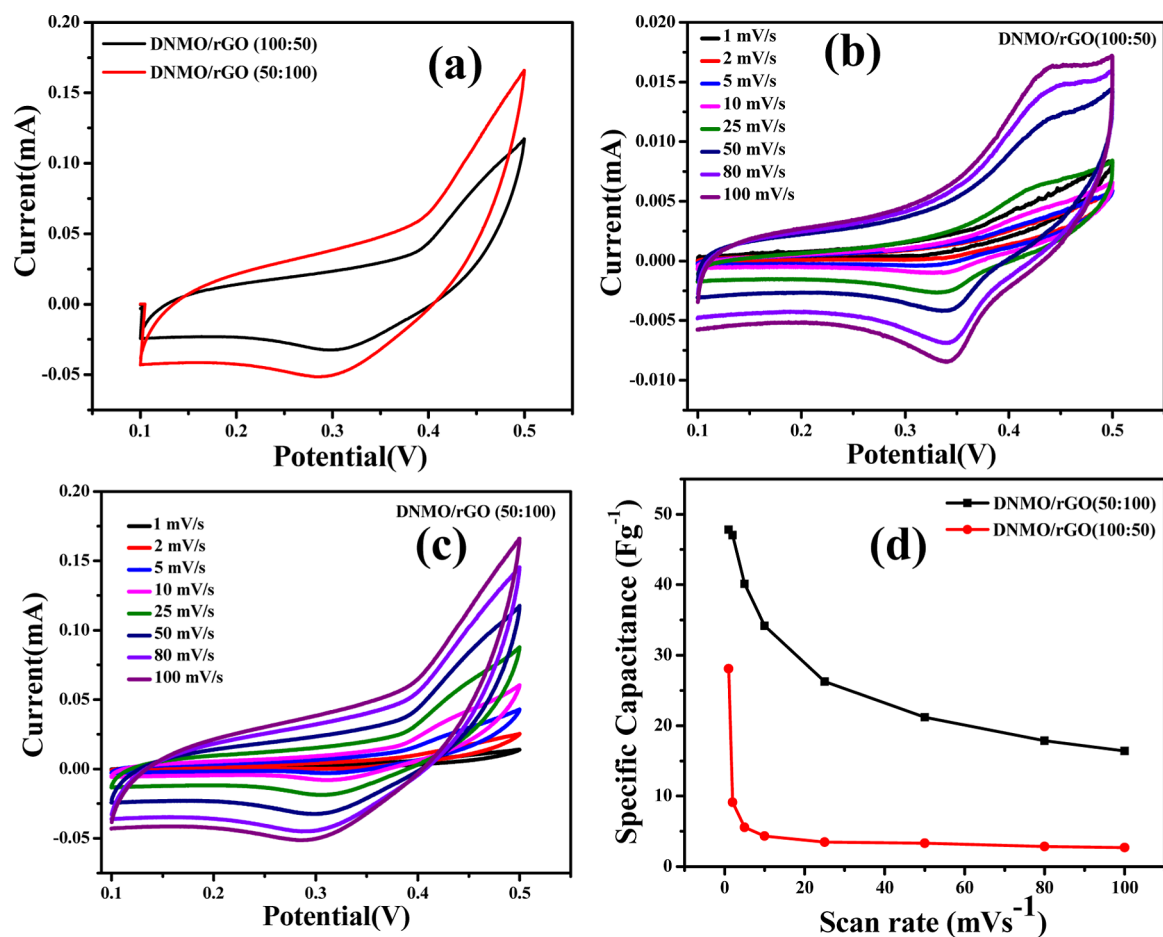
Figure 8. (a) Comparison CV curves of DNMO/rGO (50:100) and DNMO/rGO (100:50) nanocomposites at scan rates of 100 mV s^{-1}. CV curves of (b) DNMO/rGO (100:50) and (c) DNMO/rGO (50:100) nanocomposites at scan rates of 1,2, 5, 10, 25, 50, 80, and 100 mV s^{-1}, respectively. (d) Specific capacitance value of DNMO/rGO (50:100) and DNMO/rGO (100:50) nanocomposites at various scan rates.

As shown in Figure 8d, the highest specific capacitance calculated from CV curves is 48 F/g for the DNMO/rGO (50/100) electrode as compared to DNMO/rGO (100/50) (29 F/g) at a scan rate of 1 mV s^{-1}. The increase in specific capacitance of DNMO/rGO (50/100) nanocomposite as compared to DNMO/rGO (100/50) nanocomposite is due to the higher content of rGO, which increase the surface area of the active electrode and improve the conductivity of the electrode that leads to easy migration of electrolytic ions and electron transfer through the electrode and the electrode/electrolyte interface.[50,51]

In order to further investigate the cyclic stability, the multiple CV cycles using the best performing material, DNMO/rGO (50:100), have been investigated, and the results are shown in Figure 9a, the CV plots remained stable up to 300 cycles when the potential is scanned up to 0.65 V. The peak in the CV plots at 0.1 and 0.45 V are the typical redox signatures of the Ni and Mn redox centers. The redox responses are cycled very well in multiple charge–discharge cycles as recorded up to 300 cycles. Similarly, the galvanostatic charge and discharge (GCD) multiple cycles are recorded and shown in Figure 9b for the DNMO/rGO (50:100) electrode. The performance of the electrode is observed to be reproducible in multiple cycles. The specific capacitance of the DNMO/rGO (50:100) composite electrode is measured from the GCD plots and the gravimetric specific capacitance is obtained as 260 F/g, when recorded at the current density of 1 A/g. The CV

performance of DNMO/rGO (50:100) is compared with that of bare DNMO and plots are shown in Figure 9c. Inclusion of rGO at the DNMO/rGO ratio at (50:100) has shown significant improvement in performance compared to the bare DNMO electrode. In order to further explain the enhancement in the performance of the DNMO upon inclusion of rGO, the electrochemical impedance spectroscopy experiments are carried out and the resulting Nyquist plots are shown in Figure 9d along with the equivalent circuit as inset of the Figure 9d The series resistance across all the materials remained similar, however the charge transfer resistance is observed to decreased significantly when rGO is incorporated with DNMO and the composite electrode is formed. The charge transfer resistance is relatively lower in the DNMO/rGO (50:100) composite compared to the DNMO/rGO (100:50) composite. The Warburg resistive component W has been observed at the low frequency part of the Nyquist plot for all the material, indicating the porous nature of DNMO and diffusion through the pores have contribution toward the charge rearrangements.

4. CONCLUSIONS

In this study, DNMO/rGO nanocomposites have been successfully synthesized through two-step sol–gel and solvothermal processes and studied their catalytic, EMI shielding, and electrochemical properties. The structural and morphological features of the DNMO/rGO nanocomposites
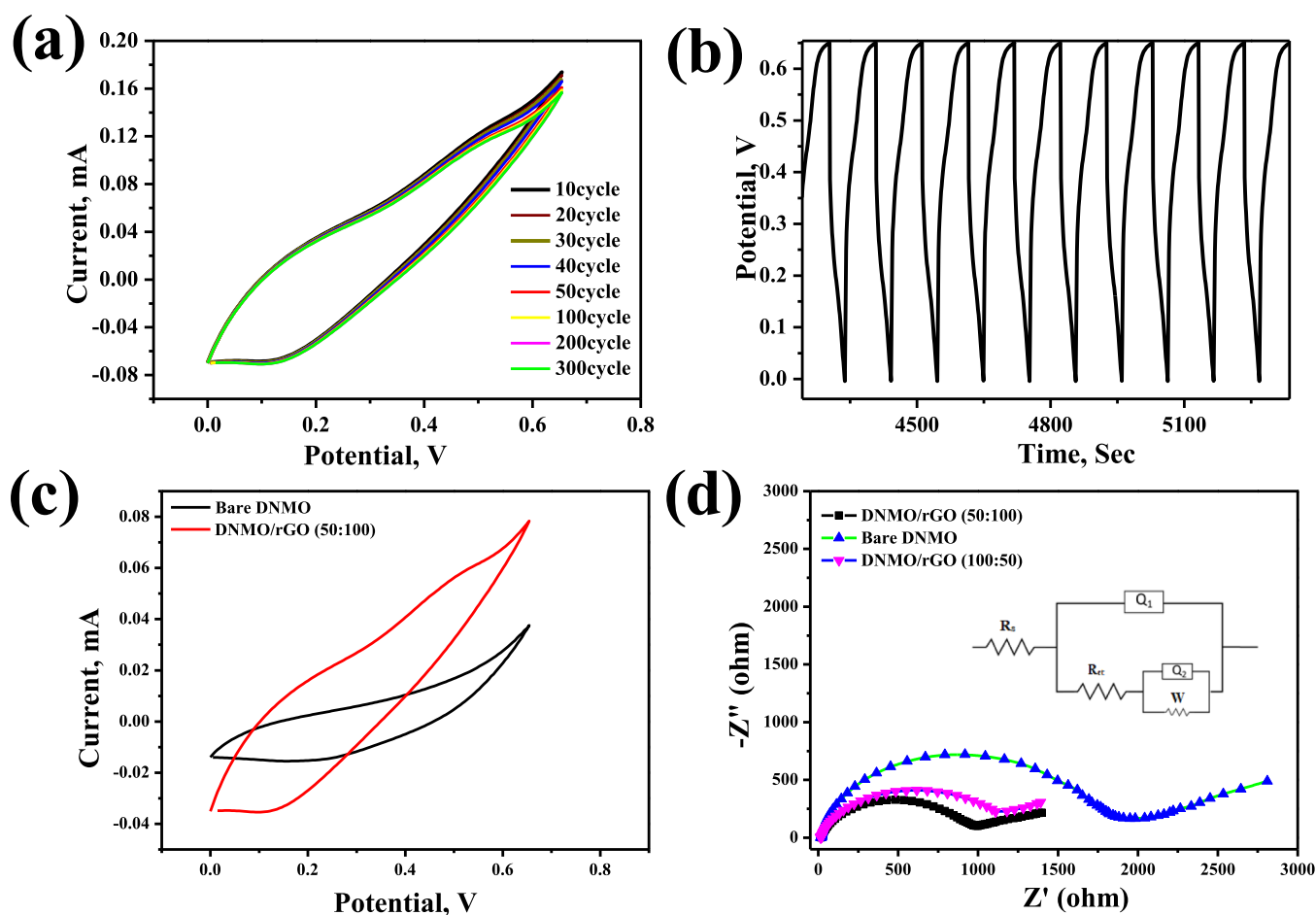
Figure 9. (a) Electrochemical CV curves vs cycle number for the DNMO/rGO (50:100) recorded over 300th cycles at 100 mV s^{-1} scan rate, (b) GCD curves of the DNMO/rGO (50:100) at a current density of 1 A g^{-1}, (c) comparison CV curves of bare DNMO and DNMO/rGO (50:100) at a scan rate of 50 mV s^{-1}, and (d) Nyquist plots of bare DNMO, DNMO/rGO (50:100), and DNMO/rGO (100:50) in the frequency range from 0.1 Hz to 50 kHz at open circuit potential (inset shows the electrochemical equivalent circuit).

were studied by XRD, Raman, XPS, FEG-SEM, and EDX characterization techniques. Catalytic activity toward 4-NP reduction was significantly improved by the incorporation of rGO into DNMO to form non-noble DNMO/rGO nanocatalysts, and the rate of reduction is susceptible to the composition of DNMO/rGO nanocomposites. Furthermore, the DNMO/rGO nanocomposite shows an excellent EMI shielding effectiveness of 6 dB with 75% attenuation at a frequency of 8.5 GHz as compared to bare DNMO and can be adopted as radar-absorbing material in civil and military applications. Electrochemical performance of DNMO/rGO nanocomposites were investigated as electrode materials for supercapacitors, and showed a maximum specific capacitance of 260 F/g at 1 A/g, specific capacitance has been significantly improved by the incorporation of rGO into DNMO. The as-produced multifunctional nanocomposites could be employed as a promising novel material and hold potential candidates for various unexplored domains, including sensors, electrocatalysis, photocatalysis, biomedicine, and environmental protection applications.

■ AUTHOR INFORMATION

Corresponding Authors

Prasanta Kumar Sahoo − *Department of Mechanical Engineering, Siksha "O" Anusandhan, Deemed to Be University, Bhubaneswar, Odisha 751030, India; Environmental Hydrology Division, National Institute of Hydrology, Jalvigyan Bhawan, Roorkee 247667, India;* ⓘ orcid.org/0000-0001-8003-9471; Email: prasantakumarsahoo@soa.ac.in

Chuan-Pei Lee − *Department of Applied Physics and Chemistry, University of Taipei, Taipei 10048, Taiwan;* Email: cplee@utaipei.edu.tw

Authors

Bibhuti Bhusan Sahoo − *Department of Mechanical Engineering, Siksha "O" Anusandhan, Deemed to Be University, Bhubaneswar, Odisha 751030, India*

Vijayabhaskara Rao Bhaviripudi − *Department of Physics, Defence Institute of Advanced Technology, Pune, Maharashtra 411025, India; Departamento de Ingeniería Química, Biotecnología y Materiales, FCFM, Universidad de Chile, Santiago 8370415, Chile*

Krushna Chandra Sahu − *Department of Chemistry, Siksha 'O' Anusandhan, Deemed to be University, Bhubaneswar, Odisha 751030, India*

Abhishek Tripathi − *Department of Metallurgical and Materials Engineering, Malaviya National Institute of Technology Jaipur, Jaipur 302017, India*

Naresh Kumar Sahoo − *Department of Chemistry, Siksha 'O' Anusandhan, Deemed to be University, Bhubaneswar, Odisha 751030, India*

Radhamanohar Aepuru − *Departamento de Mecanica, Facultad de Ingeniería, Universidad Tecnológica Metropolitana, Santiago 7800002, Chile*

Vishwajit M. Gaikwad − *Department of Physics, Amolakchand Mahavidyalaya, Yavatmal, Maharashtra 445001, India;* ⬤ orcid.org/0000-0002-2322-7000

Srikant Sahoo − *Analytical Chemistry Division, Bhabha Atomic Research Centre, Trombay, Mumbai 400085, India*

Ashis Kumar Satpati − *Analytical Chemistry Division, Bhabha Atomic Research Centre, Trombay, Mumbai 400085, India;* ⬤ orcid.org/0000-0002-2732-8706

Complete contact information is available at:
https://pubs.acs.org/10.1021/acsomega.3c07759

Author Contributions

◆B.B.S. and P.K.S. contributed equally to this work.

Notes

The authors declare no competing financial interest.

■ REFERENCES

(1) Preeti; Banerjee, S.; Debnath, A.; Singh, V. Gum ghatti-alginate hybrid bead derived titania spheres for deep removal of toxic dye Remazol Brilliant Violet from aqueous solutions. *Environ. Nanotechnol. Monit. Manag.* **2021**, *15*, 100459.

(2) Shukla, V. Review of electromagnetic interference shielding materials fabricated by iron ingredients. *Nanoscale Adv.* **2019**, *1*, 1640−1671.

(3) Simon, P.; Gogotsi, Y. Materials for electrochemical capacitors. *Nat. Mater.* **2008**, *7*, 845−854.

(4) Zeng, J.; Zhang, Q.; Chen, J.; Xia, Y. A. A Comparison Study of the Catalytic Properties of Au-Based Nanocages, Nanoboxes, and Nanoparticles. *Nano Lett.* **2010**, *10*, 30−35.

(5) Panigrahy, B.; Sahoo, P. K.; Sahoo, B. B. Construction of CdSe-AuPd quantum dot 0D/0D hybrid photocatalysts: charge transfer dynamic study with electrochemical analysis for improved photocatalytic activity. *Dalton Trans.* **2022**, *51*, 664−674.

(6) Bhaskara Rao, B. V.; Yadav, P.; Aepuru, R.; Panda, H. S. P.; Ogale, S.; Kale, S. N. Single-layer graphene-assembled 3D porous carbon composites with PVA and Fe_3O_4 nano-fillers: an interface-mediated superior dielectric and EMI. *Phys. Chem. Chem. Phys.* **2015**, *17*, 18353−18363.

(7) Sahoo, P. K.; Kumar, N.; Thiyagarajan, S.; Thakur, D.; Panda, H. S. Freeze-Casting of Multifunctional Cellular 3D-Graphene/Ag Nanocomposites: Synergistically Affect Supercapacitor, Catalytic, and Antibacterial Properties. *ACS Sustainable Chem. Eng.* **2018**, *6*, 7475−7487.

(8) Sahoo, P. K.; Aepuru, R.; Panda, H. S.; Bahadur, D. Ice-templated synthesis of multifunctional three-dimensional graphene/noble metal nanocomposites and their mechanical, electrical, catalytic and electromagnetic shielding properties. *Sci. Rep.* **2015**, *5*, 17726.

(9) Kumar Sahoo, P.; Panigrahy, B.; Thakur, D.; Bahadur, D. Ice-templating synthesis of macroporous noble metal/3D-graphene nanocomposites: their fluorescence lifetimes and catalytic study. *New J. Chem.* **2017**, *41*, 7861−7869.

(10) Banerjee, S.; Debnath, A.; Allam, B. K.; Musa, N. Adsorptive and photocatalytic performance of perovskite material for the removal of food dye in an aqueous solution. *Environ. Challenges* **2021**, *5*, 100240.

(11) Zhong, W.; Jiang, T.; Dang, Y.; He, J.; Chen, S.-Y.; Kuo, C.-H.; Kriz, D.; Meng, Y.; Meguerdichian, A. G.; Suib, S. L. Mechanism studies on methyl orange dye degradation by perovskite-type $LaNiO_{3-\delta}$ under dark ambient conditions. *Appl. Catal., A* **2018**, *549*, 302−309.

(12) Psathas, P.; Georgiou, Y.; Moularas, C.; Armatas, G. S.; Deligiannakis, Y. Controlled-Phase Synthesis of $Bi_2Fe_4O_9$ & $BiFeO_3$ by Flame Spray Pyrolysis and their evaluation as non-noble metal catalysts for efficient reduction of 4-nitrophenol. *Powder Technol.* **2020**, *368*, 268−277.

(13) Mhlwatika, Z.; Bingwa, N. Kinetic evaluation of perovskites-type catalysts in the reduction of 4-nitrophenol: A mechanistic elucidation study. *Inorg. Chem. Commun.* **2022**, *144*, 109920.

(14) Gaikwad, V. M.; Dash, B. B.; Sahoo, P. K.; Shirbhate, S. C.; Pabba, D. P.; Acharya, S. A.; Lad, A. B.; Nayak, A. K.; Viswanathan, M. R.; Aepuru, R. Polarization induced ferroelectric and magnetic ordering in double-perovskite-based flexible 0−3 composite. *J. Mater. Sci. Mater. Electron.* **2023**, *34*, 720.

(15) Xu, W.; Pan, Y. F.; Wei, W.; Wang, G. S. Nanocomposites of Oriented Nickel Chains with Tunable Magnetic Properties for High-Performance Broadband Microwave Absorption. *ACS Appl. Nano Mater.* **2018**, *1* (3), 1116−1123.

(16) Liu, X.; Wang, L.-S.; Ma, Y.; Zheng, H.; Lin, L.; Zhang, Q.; Chen, Y.; Qiu, Y.; Peng, D.-L. Enhanced Microwave Absorption Properties by Tuning Cation Deficiency of Perovskite Oxides of Two-Dimensional $LaFeO_3$/C Composite in X-Band. *ACS Appl. Mater. Interfaces* **2017**, *9*, 7601−7610.

(17) Dijith, K. S.; Pillai, S.; Surendran, K. P. Screen printed silver patterns on $La_{0.5}Sr_{0.5}CoO_{3-\delta}$—Epoxy composite as a strategy for many-fold increase in EMI shielding. *Surf. Coat. Technol.* **2017**, *330*, 34−41.

(18) Sharma, G. K.; James, N. R. Flexible N-Doped Carbon Nanofiber-Polydimethylsiloxane Composite Containing $La_{0.85}Sr_{0.15}CoO_{3-\delta}$ Nanoparticles for Green EMI Shielding. *ACS Appl. Nano Mater.* **2023**, *6*, 6024−6035.

(19) Kumar, R.; Sahoo, S.; Joanni, E.; Singh, R.; Tan, W. K.; Kar, K. K.; Matsuda, A. Recent progress on carbon-based composite materials for microwave electromagnetic interference shielding. *Carbon* **2021**, *177*, 304−331.

(20) Kumar, R.; Sahoo, S.; Joanni, E. Composites based on layered materials for absorption of microwaves and electromagnetic shielding. *Carbon* **2023**, *211*, 118072.

(21) Kumar, R.; Sahoo, S.; Joanni, E.; Singh, R. K.; Tan, W. K.; Moshkalev, S. A.; Matsuda, A.; Kar, K. K. Heteroatom doping of 2D graphene materials for electromagnetic interference shielding: a review of recent progress. *Crit. Rev. Solid State Mater. Sci.* **2022**, *47* (4), 570−619.

(22) Kumar, R.; Alaferdov, A. V.; Singh, R. K.; Singh, A. K.; Shah, J.; Kotnala, R. K.; Singh, K.; Suda, Y.; Moshkalev, S. A. Self-assembled nanostructures of 3D hierarchical faceted-iron oxide containing vertical carbon nanotubes on reduced graphene oxide hybrids for enhanced electromagnetic interface shielding. *Composites, Part B* **2019**, *168*, 66−76.

(23) Mu, X.; Du, J.; Zhang, Y.; Liang, Z.; Wang, H.; Huang, B.; Zhou, J.; Pan, X.; Zhang, Z.; Xie, E. Construction of hierarchical CNT/rGO-supported $MnMoO_4$ nanosheets on Ni foam for high-performance aqueous hybrid supercapacitors. *ACS Appl. Mater. Interfaces* **2017**, *9*, 35775−35784.

(24) Han, X.; Tao, K.; Wang, D.; Han, L. Design of a porous cobalt sulfide nanosheet array on Ni foam from zeolitic imidazolate frameworks as an advanced electrode for supercapacitors. *Nanoscale* **2018**, *10*, 2735−2741.

(25) Zhang, J.; Zhao, X. S. On the configuration of supercapacitors for maximizing electrochemical performance. *ChemSusChem* **2012**, *5*, 818−841.

(26) Cheng, M.; Fan, H.; Xu, Y.; Wang, R.; Zhang, X. Hollow Co_2P nanoflowers assembled from nanorods for ultralong cycle-life supercapacitors. *Nanoscale* **2017**, *9*, 14162−14171.

(27) Xia, X.; Zhan, J.; Zhong, Y.; Wang, X.; Tu, J.; Fan, H. J. Single-crystalline, metallic TiC nanowires for highly robust and wide-temperature electrochemical energy storage. *Small* **2017**, *13*, 1602742.

(28) Kumar, R.; Sahoo, S.; Joanni, E.; Singh, R. K.; Kar, K. K. Microwave as a Tool for Synthesis of Carbon-Based Electrodes for Energy Storage. *ACS Appl. Mater. Interfaces* **2022**, *14* (18), 20306−20325.

(29) Tan, P.; Liu, M.; Shao, Z.; Ni, M. Recent advances in perovskite oxides as electrode materials for nonaqueous lithium-oxygen batteries. *Adv. Energy Mater.* **2017**, *7*, 1602674.

(30) Xu, X.; Wang, W.; Zhou, W.; Shao, Z. Recent advances in novel nanostructuring methods of perovskite electrocatalysts for energy-related applications. *Small Methods* **2018**, *2*, 1800071.

(31) Kumar, A.; Kumar, A. Electrochemical behavior of oxygen-deficient double perovskite, Ba2FeCoO6-δ, synthesized by facile wet chemical process. *Ceram. Int.* **2019**, *45*, 14105−14110.

(32) Muddelwar, R. K.; Pani, J.; Lad, A. B.; Kumar, K. U.; Gaikwad, V. M.; Borkar, H. Pr_2CrMnO_6 double perovskite as new electrode material for electrochemical energy storage. *Mater. Chem. Phys.* **2023**, *302*, 127726.

(33) Alam, M.; Karmakar, K.; Pal, M.; Mandal, K. Electrochemical supercapacitor based on double perovskite Y_2NiMnO_6 nanowires. *RSC Adv.* **2016**, *6*, 114722−114726.

(34) Zhang, L.; Zhang, F.; Yang, X.; Long, G.; Wu, Y.; Zhang, T.; Leng, K.; Huang, Y.; Ma, Y.; Yu, A.; et al. Porous 3D graphene-based bulk materials with exceptional high surface area and excellent conductivity for supercapacitors. *Sci. Rep.* **2013**, *3*, 1408−1409.

(35) Sahoo, P. K.; Sahoo, S.; Satpati, A. K.; Bahadur, D. Solvothermal synthesis of reduced graphene oxide/Au nanocomposite-modified electrode for the determination of inorganic mercury and electrochemical oxidation of toxic phenolic compounds. *Electrochem. Acta* **2015**, *180*, 1023−1032.

(36) Gaikwad, V. M.; Dash, B. B.; Sahoo, P. K.; Shirbhate, S. C.; Pabba, D. P.; Acharya, S. A.; Lad, A. B.; Nayak, A. K.; Viswanathan, M. R.; Aepuru, R. Polarization induced ferroelectric and magnetic ordering in double-perovskite-based flexible 0−3 composite. *J. Mater. Sci.: Mater. Electron.* **2023**, *34*, 720.

(37) Sahoo, P. K.; Thakur, D.; Bahadur, D.; Panigrahy, B. Highly efficient and simultaneous catalytic reduction of multiple dyes using recyclable RGO/Co dendritic nanocomposites as catalyst for wastewater treatment. *RSC Adv.* **2016**, *6*, 106723−106731.

(38) Sahoo, B. B.; Kumar, N.; Panda, H. S.; Panigrahy, B.; Sahoo, N. K.; Soam, A.; Mahanto, B. S.; Sahoo, P. K. Self-assembled 3D graphene-based aerogel with Au nanoparticles as high-performance supercapacitor electrode. *J. Energy Storage* **2021**, *43*, 103157.

(39) Barreca, D.; Gasparotto, A.; Milanov, A.; Tondello, E.; Devi, A.; Fischer, R. A. Nanostructured Dy_2O_3 films: An XPS investigation. *Surf. Sci. Spectra* **2007**, *14*, 52−59.

(40) Pana, O.; Soran, M. L.; Leostean, C.; Macavei, S.; Gautron, E.; Teodorescu, C. M.; Gheorghe, N.; Chauvet, O. Interface charge transfer in polypyrrole coated perovskite Manganite magnetic nanoparticles. *J. Appl. Phys.* **2012**, *111*, 044309.

(41) Xie, T.; Min, J.; Liu, J.; Chen, J.; Fu, D.; Zhang, R.; Zhu, K.; Lei, M. Synthesis of mesoporous Co_3O_4 nanosheet-assembled hollow spheres towards efficient electrocatalytic oxygen evolution. *J. Alloys Compd.* **2018**, *754*, 72−77.

(42) Kuroda, K.; Ishida, T.; Haruta, M. Reduction of 4-nitrophenol to 4-aminophenol over Au nanoparticles deposited on PMMA. *J. Mol. Catal. A: Chem.* **2009**, *298*, 7−11.

(43) Huang, H.; Yang, S.; Vajtai, R.; Wang, X.; Ajayan, P. M. Pt-decorated 3D architectures built from graphene and graphitic carbon nitride nanosheets as efficient methanol oxidation catalysts. *Adv. Mater.* **2014**, *26*, 5160−5165.

(44) Hassan, M.; Haque, E.; Reddy, K. R.; Minett, A. I.; Chen, J.; Gomes, V. G. Edge-enriched graphene quantum dots for enhanced photo-luminescence and supercapacitance. *Nanoscale* **2014**, *6*, 11988−11994.

(45) Aepuru, R.; Ramalinga Viswanathan, M.; Rao, B. B.; Panda, H. S.; Sahu, S.; Sahoo, P. K. Tailoring the performance of mechanically robust highly conducting Silver/3D graphene aerogels with superior electromagnetic shielding effectiveness. *Diamond Relat. Mater.* **2020**, *109*, 108043.

(46) Shi, Y. D.; Li, J.; Tan, Y. J.; Chen, Y. F.; Wang, M. Percolation behavior of electromagnetic interference shielding in polymer/multi-walled carbon nanotube nanocomposites. *Compos. Sci. Technol.* **2019**, *170*, 70−76.

(47) Aepuru, R.; Ramalinga Viswanathan, M.; Rao, B. B.; Panda, H. S.; Sahu, S.; Sahoo, P. K. Tailoring the performance of mechanically robust highly conducting Silver/3D graphene aerogels with superior electromagnetic shielding effectiveness. *Diam. Relat. Mater.* **2020**, *109*, 108043.

(48) Bhaskara Rao, B.; Jena, M.; Aepuru, R.; Udayabhaskar, R.; Ramalinga Viswanathan, M.; Gonzalez, R. E.; Kale, S. N. Superior electromagnetic wave absorption performance of Fe_3O_4 modified graphene assembled porous carbon (mGAPC) based hybrid foam. *Mater. Chem. Phys.* **2022**, *290*, 126512.

(49) Kumar, N.; Ghosh, S.; Thakur, D.; Lee, C. P.; Sahoo, P. K. Recent advancements in zero- to three-dimensional carbon networks with a two-dimensional electrode material for high-performance supercapacitors. *Nanoscale Adv.* **2023**, *5*, 3146−3176.

(50) Anandhi, P.; Harikrishnan, S.; Senthil Kumar, V. J.; Lai, W. C.; Mahmoud, A. E. D. The Enhanced Energy Density of rGO/TiO_2 Based Nanocomposite as Electrode Material for Supercapacitor. *Electronics* **2022**, *11*, 1792.

(51) Lakra, R.; Mahender, C.; Singh, B. K.; Kumar, R.; Kumar, S.; Sahoo, P. K.; Thatoi, D.; Soam, A. $ZnFe_2O_4$ Nanoparticles Supported on Graphene Nanosheets for High-Performance Supercapacitor. *J. Electron. Mater.* **2023**, *52*, 2676−2684.